Journal of Materials Chemistry A

ROYAL SOCIETY OF CHEMISTRY

PAPER

View Article Online
View Journal | View Issue

Cite this: J. Mater. Chem. A, 2022, 10, 10439

Mechanistic insights into the pseudocapacitive performance of bronze-type vanadium dioxide with mono/multi-valent cations intercalation†

Ying Zeng,‡[a] Jian Hu,‡[ab] Jiaofeng Yang,[c] Pei Tang,[a] Qingfeng Fu,[a] Wang Zhou,[a] Yufan Peng,[a] Peitao Xiao,[d] Shi Chen,[e] Kunkun Guo,[a] Peng Gao,*[a] Hongliang Dong*[fg] and Jilei Liu*[a]

Bronze-type vanadium dioxide (VO_2(B)) is a promising intercalation pseudocapacitive material due to its special corner and edge-sharing structure. Meanwhile, the utilization of multivalent cations as charge carriers has been considered an effective strategy to further improve its charge storage capability. However, the mechanistic understanding of multivalent cations' intercalation into VO_2(B) is still vague, which greatly limits its practical application. *Via* a combination of structure characterization, theoretical calculations and electrochemical analysis, we have shown that only ion (de-)intercalation into VO_2(B) occurs in Na_2SO_4 and $MgSO_4$ electrolytes upon cycling, and their distinct charge storage performance is considered due to the synergistic effects between the ionic radius of electrolyte cations and their polarizing power. In contrast, part of VO_2(B) is reversibly converted to $Zn_3(OH)_2V_2O_7{\cdot}2H_2O$ in $ZnSO_4$ electrolyte, followed by Zn^{2+} (de-)intercalation into both phases upon cycling, thus enabling full utilization of the bulk electrode and realizing maximization of the specific capacitance (460 F g^{-1} at 1 A g^{-1} current density). When cycled in $Al_2(SO_4)_3$ electrolyte, the large VO_2(B) nanobelts collapse into small pellets due to the strong electrostatic force between the Al^{3+} ions and host structure, thereby resulting in serious structural instability and inferior pseudocapacitive properties. In general, this work provides valuable insights in understanding the behaviors of mono/multi-valent cations upon intercalation into VO_2(B), which will enable rational design of more layered oxides with excellent charge storage properties or will be extended to other applications.

Received 27th January 2022
Accepted 10th April 2022

DOI: 10.1039/d2ta00760f

rsc.li/materials-a

1. Introduction

In recent years, the increasing demand for electric vehicles and renewable energy sources has promoted the development of efficient electrical energy storage (EES) devices with a combination of high energy density, high power density and good cycle performance.[1–4] Intercalation pseudocapacitors, which typically involve electrolyte ion insertion into the layers/tunnels of the electrode materials accompanied by faradaic charge-transfer, are promising candidates for realizing enhanced charge storage capability and may bridge the gap between batteries and electrical double-layer capacitors.[5–7] Two-dimensional (2D) materials, such as manganese dioxide (MnO_2) and vanadium pentoxide (V_2O_5), are typical intercalation pseudocapacitive materials due to their facile ion intercalation channels that enable full utilization of the bulk electrode. However, the unstable host structure upon cycling due to the weak van der Waals interactions between adjacent layers limits their cycle performance.[8] Therefore, seeking electrode materials with a robust structure is extremely necessary. VO_2(B), a metastable monoclinic polymorph of vanadium oxides, has emerged as a promising candidate recently due to its special structure as

[a]College of Materials Science and Engineering, Hunan Joint International Laboratory of Advanced Materials and Technology for Clean Energy, Hunan Province Key Laboratory for Advanced Carbon Materials and Applied Technology, Hunan University, Changsha 410082, China. E-mail: gaop@hnu.edu.cn; liujilei@hnu.edu.cn

[b]Hunan Provincial Key Laboratory of Fine Ceramics and Powder Materials, School of Materials and Environmental Engineering, Hunan University of Humanities, Science and Technology, Loudi, Hunan 417000, China

[c]Hunan Communications Research Institute Co. Ltd, Changsha 410015, China

[d]Department of Materials Science and Engineering, National University of Defense Technology, Changsha, Hunan, 410073, China

[e]Joint Key Laboratory of the Ministry of Education, Institute of Applied Physics and Materials Engineering, University of Macau, Avenida da Universidade, Taipa, Macau 999078, China

[f]Center for High Pressure Science and Technology Advanced Research, Pudong, Shanghai 201203, China. E-mail: hongliang.dong@hpstar.ac.cn

[g]State Key Laboratory of High Performance Ceramics and Superfine Microstructure, Shanghai Institute of Ceramics, Chinese Academy of Sciences, Shanghai 201899, China

† Electronic supplementary information (ESI) available. See https://doi.org/10.1039/d2ta00760f

‡ These authors contributed equally to this article.

well as its low cost, natural abundance and easy fabrication.[9–13] The crystal structure of VO_2(B), comprising sheets of distorted edge-sharing VO_6 octahedra that are linked to adjacent sheets by corner sharing along the *c*-direction, is shown in Fig. 1(a). Unlike other layered oxides, the corner and edge sharing motif of VO_2(B) is resistant to lattice shearing upon cation intercalation, thus leading to a quite stable structure during electrochemical cycling.[14–16] Meanwhile, the large-sized tunnel along the *b*-axis is beneficial for fast ion insertion/extraction in VO_2(B), and may therefore also ensure good rate performance and high power density.[17,18]

Generally speaking, VO_2(B)-based pseudocapacitors are operated in water electrolyte, meaning that the potential window of the device is limited by water electrolysis. Therefore, the preparation of electrodes with high capacitance is needed to achieve high energy density (according to the formula $E = 1/2CV^2$, where E is the energy density, C is the specific capacitance of the electrode material, and V is the potential window of the device).[19–21] Aside from the commonly used methods including morphology control[22–24] and forming composites with conductive substances,[25–27] another effective strategy that has recently emerged is to use multivalent cations (such as Zn^{2+}, Mg^{2+}, Al^{3+}, *etc.*) as charge carriers, since they can induce multi-electron transfers upon cycling compared to those of monovalent cations (such as Li^+, Na^+, and K^+) and have been confirmed to be promising in aqueous rechargeable batteries.[28–33] For example, Yang *et al.*[34] studied the pseudocapacitive behavior of Zn^{2+} upon intercalation into the tunnels of VO_2(B) nanofibers in aqueous electrolyte, and found that the limitation from solid-state diffusion in VO_2(B) is eliminated due to its unique transport pathways with large tunnel sizes and little structural change, thus leading to a high reversible capacity of 357 mA h g^{-1} and excellent rate capability (171 mA h g^{-1} at 300C). Cheng *et al.*[35] investigated the zinc storage mechanisms in VO_2(B) over a large voltage range, and demonstrated that the VO_2(B) undergoes an irreversible conversion reaction when the potential approaches

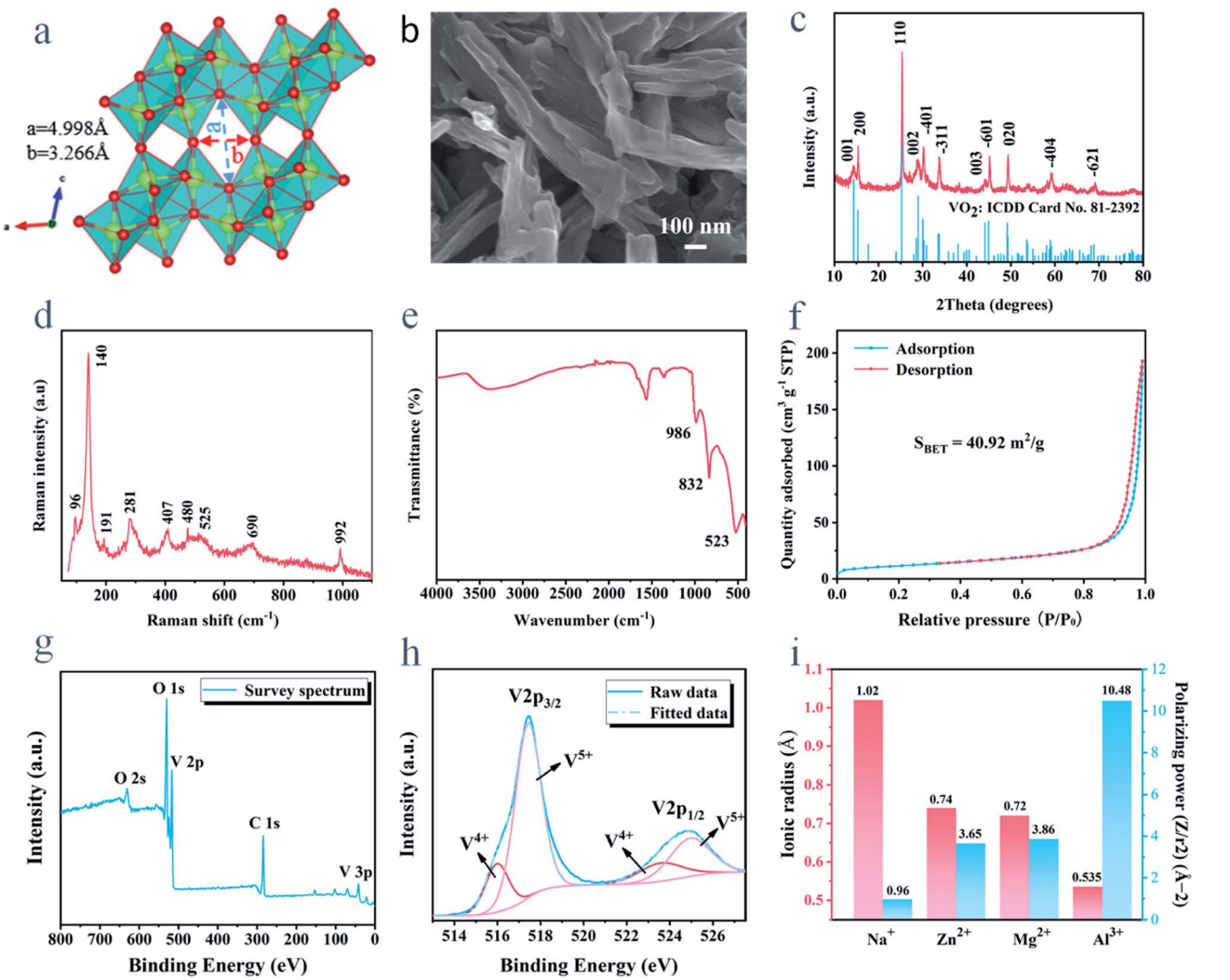

Fig. 1 (a) Crystal structure, (b) SEM image, (c) XRD pattern, (d) Raman spectrum, (e) FTIR spectrum, (f) N_2 adsorption–desorption isotherm, (g) XPS survey scan, and (h) high-resolution V 2p spectra of the as-prepared VO_2(B). (i) Ionic radius and polarizing power comparison of Na^+, Mg^{2+}, Zn^{2+} and Al^{3+} ions.

~1.5 V. The conversion product shows a high zinc ion storage capacity of 330 mA h g^{-1} at 0.1 A g^{-1} and high rate performance (130 mA h g^{-1} at 10 A g^{-1}). Srinivasan *et al.*[36] prepared holey VO_2(B) nanobelts as the cathode material for aqueous aluminum-ion batteries. The electrode delivers a superior specific capacity of up to 234 mA h g^{-1} at 150 mA g^{-1} and exhibits a high capacity retention of 77.2% over 1000 cycles at 1 A g^{-1}. Moreover, Hu *et al.* have conducted a series of experiments on elucidating the charge storage mechanisms of various vanadium oxides in aqueous electrolytes containing Li^+, Na^+ and K^+ ions, including the effects of lithium concentration on $VO_x \cdot yH_2O$'s rate performance,[37] the influences of an intrinsic porous and crystalline structure on hydrous vanadium oxide's power characteristics,[38] and the novel redox intercalation ability and ion selectivity for potassium among Li, Na and K ions of hydrothermally prepared $V_2O_5 \cdot 1.9H_2O$.[39] Other than that, to the best of our knowledge, little information about the behaviors of multivalent cations upon intercalation into VO_2(B)-based pseudocapacitive electrodes is available.

Herein, we have systematically investigated the behaviors of Na^+, Mg^{2+}, Zn^{2+}, and Al^{3+} ions (which exhibit distinct physicochemical properties including different charge numbers per ion (Z), ionic radii (r) and polarizing power (a parameter (Z/r^2) that can be interpreted as a measure of the strength of the charge field that affects the neighboring atoms[40]), along with their natural abundance and low price) upon intercalation into solvothermally prepared VO_2(B). By combining a series of structure characterization experiments, theoretical calculations and electrochemical analysis, we found that (i) only ion (de-)intercalation into the tunnels occurs when VO_2(B) is cycled in Na_2SO_4 and $MgSO_4$ electrolytes; meanwhile, their distinct electrochemical behaviors are affected by the synergistic effects between the ionic radius of electrolyte cations and their polarizing power, (ii) part of the VO_2(B) is reversibly converted to $Zn_3(OH)_2V_2O_7 \cdot 2H_2O$ when added to $ZnSO_4$ electrolyte, followed by Zn^{2+} (de-)intercalation into both phases upon cycling, which enables full utilization of the bulk electrode, thereby realizing superior specific capacitance (460 F g^{-1} at 1 A g^{-1} current density), and (iii) when cycled in $Al_2(SO_4)_3$ electrolyte, the large VO_2(B) nanobelts collapse into small pellets which is mainly attributed to the strong electrostatic force between Al^{3+} ions and the host structure, thereby resulting in serious structural instability and inferior pseudocapacitive properties. In general, our detailed comparative studies provide valuable insights in elucidating the behaviors of mono/multi-valent cations upon intercalation into VO_2(B), which is beneficial for the rational design of more layered oxides with excellent electrochemical performance.

2. Methods

2.1 Chemicals and reagents

Vanadium pentoxide (V_2O_5), ethylene glycol (EG), sodium sulfate (Na_2SO_4), magnesium sulfate ($MgSO_4$), zinc sulfate ($ZnSO_4$), aluminum sulfate ($Al_2(SO_4)_3$), hydrochloric acid (HCl), acetone (>99.5%) and ethanol (99.5%) were purchased from commercial suppliers (Sinopharm Chemical Reagent Co., Ltd). All chemicals were used as received without further purification.

2.2 Preparation of VO_2(B) nanobelts

VO_2(B) nanobelts were obtained *via* a facile one-step solvothermal alcohol reduction reaction of V_2O_5. In a typical synthesis procedure, 4 mmol V_2O_5 was dispersed in 50 mL of water/ethylene glycol (volume ratio: 3 : 2) mixture under vigorous stirring for 30 min, which was then transferred into a 100 mL Teflon-lined stainless steel autoclave and kept in an oven at 200 °C for 6 h. After the reaction, the as-prepared product was thoroughly washed with distilled water and ethanol several times and then dried in an oven overnight at 80 °C. The solvothermal reaction conditions, including the volume ratio of water/ethylene glycol and reaction time, were also adjusted to optimize the pseudocapacitive performance of the as-synthesized VO_2(B) electrodes.

2.3 Material characterization

The as-prepared samples were characterized by powder X-ray diffraction (XRD) using a Bruker D8 Advance with Cu Kα radiation (λ = 1.5418 Å) in the 10–80° 2θ range at a scan rate of 5° min^{-1}. Surface morphologies were observed using scanning electron microscopy (SEM, Zeiss ∑IGMA HD). The structure of the as-prepared sample was investigated by high-resolution transmission electron microscopy (HRTEM, FEI Tecnai F20) operated at an acceleration voltage of 200 kV. The specific surface area was obtained by nitrogen adsorption and desorption isotherms collected on a JW-BK200 gas adsorption analyzer (Beijing JWGB SCI&TECH). X-ray photoelectron spectroscopy (XPS) was conducted using a Thermo Scientific K-Alpha XPS instrument to investigate the local chemical environment of the samples, and the spectra were calibrated using the C 1s peak. Fourier-transform infrared (FTIR) spectra were obtained using a Nicolet iS50 spectrometer (Thermo Fisher Scientific, USA) in the range of 400–4000 cm^{-1} with an attenuated total reflectance detector. Raman spectroscopy was performed with a confocal Raman microscope, WITec Alpha 300R system (WITec GmbH, Germany), at room temperature with a 532 nm wavelength incident laser light (0.3 mW laser power) and a 50× Zeiss EC Epiplan objective. Data were processed with Project FIVE+ software (Version 5.2, WITec GmbH, Germany).

2.4 Electrochemical measurements

Nickel (Ni) foam was used as a conductive substrate, and was carefully cleaned with 1 M HCl solution to remove the surface oxide layer and was then rinsed with acetone, ethanol and deionized water before use. The working electrode slurry was prepared by mixing 80 wt% active material, 10 wt% acetylene black and 10 wt% PVDF in *N*-methylpyrrolidinone (NMP) solvent, with the obtained mixture coated onto the Ni foam substrate (1 cm × 1 cm). After being dried at 80 °C in an oven overnight, the Ni foam was pressed under a pressure of 10 MPa, and then used for the electrochemical tests. The loading of the active material on the working electrode was determined by comparing the mass difference between the original and coated

Ni foams, which is typically in the range of 1.4–1.6 mg cm^{-2}. The electrochemical performances were measured using a conventional three-electrode cell in 1 M Na_2SO_4, $MgSO_4$, $ZnSO_4$ and $Al_2(SO_4)_3$ aqueous electrolytes, with Ag/AgCl and platinum foil used as the reference and auxiliary electrodes, respectively. Cyclic voltammetry (CV) scans were carried out from −0.5 to 0.6 V at various scan rates from 1 to 100 mV s^{-1} (the voltage range was set to 0–0.8 V when $Al_2(SO_4)_3$ was used as the electrolyte due to the anomalous CV curve of VO_2(B) cycled from −0.5 to 0.6 V as shown in Fig. S1†). Galvanostatic charge–discharge (GCD) was measured in the potential window of −0.5 to 0.6 V (0–0.8 V for $Al_2(SO_4)_3$ electrolyte) at different constant current densities from 1 to 10 A g^{-1}. Both the CV and GCD measurements were conducted on a Solartron analytical 1470E cell test system. Electrochemical impedance spectroscopy (EIS) measurements were performed on a Solartron impedance analyzer 1260A in the frequency range of 0.01 Hz–100 kHz at open-circuit potential with an AC perturbation amplitude of 10 mV. EIS data was fitted to an electrical equivalent circuit model using software ZView.

2.5 Computational methods

Density functional theory (DFT) calculations were carried out to examine the adsorption energy of Na, Mg, Zn and Al on VO_2(B) surfaces using the Vienna *ab initio* simulation package (VASP) code.[41] The generalized gradient approximation (GGA) was used at the PBE[42] level for functional options with spin polarized calculations. In all calculations, the cutoff energy for the plane wave basis set was fixed at 500 eV, and the self-consistent-field (SCF) calculations were repeated until both the total energy difference between two iterations and the forces on atoms converged to within 1×10^{-5} eV and less than 0.01 eV $Å^{-1}$, respectively. The vacuum thickness was set to 15 Å for all calculations, and a special $3 \times 3 \times 1$ k point of structures was chosen. The DFT-D3 [43] method with Becke–Johnson damping was applied to the calculation. The calculations for V atoms were carried out by using the GGA+U[44] approach. The U parameter has been obtained by means of a linear response method, which is 4.2 eV for the V atom. The J value was set to 0.8 eV. In the specific calculation, we selected the commonly exposed (001) surface of VO_2(B) for cutting to simulate the surface adsorbed by metal ions. Lattice parameters of VO_2(B) were $A = 12.03$ Å, $B = 3.69$ Å and $C = 6.42$ Å, and for $Zn_3(OH)_2V_2O_7$ they were $A = B = 6.05$ Å and $C = 7.19$ Å which matched the XRD results obtained from the experiment.

3. Results and discussion

3.1 Phases and microstructures

To study the intercalation behaviors of Na^+, Mg^{2+}, Zn^{2+} and Al^{3+} in VO_2(B), we first synthesized VO_2(B) nanobelts *via* a facile solvothermal approach, where the reaction conditions were optimized to obtain VO_2(B) that exhibits the best electrochemical performance (as shown in Fig. S2–S5 and Tables S1 and S2†) and was then used for further structure characterization and electrochemical evaluation. A SEM image of the as-prepared VO_2(B) nanobelts is shown in Fig. 1(b). The appearance of VO_2(B) is typical of the layer-like morphology, with platelets that may either form solvothermally or nanosheets that restack. Visible nanosheets are generally re-stacked into flat and smooth grains with some scrolling at the edges as has been reported in other studies.[4,14,45] The VO_2(B) nanobelts exhibit a large aspect ratio with a lateral size of 100–200 nm and length of 1–2 μm. Fig. 1(c) shows the XRD pattern of the as-prepared sample. All diffraction peaks are well indexed to the monoclinic structure of VO_2(B) (ICDD Card no. 81-2392) without the presence of other impurity peaks, indicating the high purity of the as-prepared sample. The color variation from yellow to dark blue (as shown in Fig. S6†) after the solvothermal reduction reaction also indicates the transformation of V_2O_5 to VO_2(B). The high-resolution TEM (HRTEM) image (Fig. S7(a)†) displays two types of interplanar distances of 0.18 and 0.21 nm, consistent with the characteristic values for d_{020} and d_{003} of monoclinic VO_2(B).[46,47] The fast Fourier transform (FFT) analysis derived from the TEM image could also be indexed to diffraction spots of monoclinic VO_2(B) indicating (020) and (003) crystal planes as shown in the inset image of Fig. S7(a).† Moreover, EDS mapping analysis (Fig. S7(b)†) unambiguously confirms the existence of V and O elements and the homogeneous profile. To further confirm the chemical compositions of the as-prepared sample, we carried out Raman measurement with the results shown in Fig. 1(d). The strong peak centered at 140 cm^{-1} is assigned to the skeleton bending vibration of the V–O–V bond and is related to the layer structures, indicating that the VO_2(B) exists in a layer-by-layer form which has been confirmed by the SEM images. The peaks located at 96, 191 and 281 cm^{-1} are attributed to the bending vibrations of V=O bonds. The peaks at 407 and 480 cm^{-1} are correlated with the bending vibrations of the bridging V–O–V. The band at 525 cm^{-1} is assigned to the stretching mode of the edge-shared O that is triply coordinated, and the band at 690 cm^{-1} corresponds to the doubly coordinated oxygen stretching mode of the corner-shared oxygen. The band at 992 cm^{-1} is attributed to the in-phase stretching vibrational mode of the apical V=O bond. All Raman peaks are in good accordance with those reported in the literature.[33,48,49] Fig. 1(e) shows the FTIR spectra of the as-prepared sample. Three distinct peaks centered at 986, 832 and 523 cm^{-1}, which stand for the symmetrical stretching modes of V^{5+}=O and V^{4+}=O, as well as the stretching mode vibration related to V–O–V in VO_2(B), are clearly observed.[33,50,51] Therefore, the above results undoubtedly confirmed that pure phase VO_2(B) nanobelts have been successfully synthesized in our experiment.

Nitrogen adsorption–desorption measurement was also performed to characterize the pore structures and obtain the specific surface area of the as-synthesized VO_2(B), with the results shown in Fig. 1(f). A well-defined type IV-like isotherm with a distinct H3-type hysteresis loop has been observed, indicating the presence of macropores and slit-like mesopores according to the IUPAC classification.[4,52,53] The Brunauer–Emmett–Teller (BET) specific surface area (SSA) of VO_2(B) is 40.9 m^2 g^{-1}, which is comparable with those reported in the literature.[13,48,54] The porous structure with a large SSA can serve as an

electrolyte reservoir and facilitates electrolyte ion infiltration, which is beneficial for improving the electrochemical charge storage performance of VO_2(B). Furthermore, the XPS measurement was applied to investigate the oxidation state of vanadium in the as-prepared VO_2(B). The survey spectrum shown in Fig. 1(g) clearly indicates the presence of vanadium and oxygen in the sample. The high-resolution V $2p_{3/2}$ peak (Fig. 1(h)) can be resolved into two peaks centered at 516.4 and 517.8 eV, which correspond to V^{4+} and V^{5+}, respectively,[13,33,55,56] and is consistent with the FTIR results. The presence of V^{5+} is either due to the incomplete reduction of vanadium during solvothermal reaction, or may be attributed to the partial oxidation of the VO_2(B) surface which is known to occur easily when vanadium ions are exposed to ambient environments and is consistent with previous reports.[14] Moreover, it is demonstrated that the mixed-valent vanadium on the surface can increase the electronic conductivity of vanadium oxides,[57,58] which is also beneficial for improving the electrochemical performance of VO_2(B) nanobelts.

3.2 Electrochemical analysis

To explore the intercalation behaviors of Na^+, Mg^{2+}, Zn^{2+} and Al^{3+} in VO_2(B), we first performed electrochemical measurements of the as-prepared electrodes in aqueous electrolyte. Fig. 2(a) shows the CV curves of VO_2(B) in different electrolytes measured at a 1 mV s^{-1} scan rate. Clearly, it can be seen that there are similar quasi-rectangular CV curves with the presence of two pairs of redox peaks when VO_2(B) is cycled in Na_2SO_4 and $MgSO_4$ electrolytes, indicating typical faradaic behaviors that correspond to the conversion between different vanadium oxidation states and multistep ion intercalation/de-intercalation processes.[14,29,32] Similarly, a pair of broad and strong redox peaks are observed when VO_2(B) is cycled in $ZnSO_4$ electrolyte. CV at different scan rates (Fig. S8,† 1–100 mV s^{-1}) was also carried out to further evaluate the intercalation behaviors of Na^+, Mg^{2+} and Zn^{2+} in VO_2(B). It is clear that the cathodic peaks shift toward higher voltages and the anodic peaks move to lower voltages with increasing scan rate owing to the polarization, a well known phenomenon consistent with previous reports.[34] Noteworthily, the Zn^{2+} intercalation leads to an obvious larger peak potential shift, a typical behavior that is related to the crystal phase changes of electrode materials upon cycling,[33,34] thus implying a different charge storage mechanism of VO_2(B) when cycled in $ZnSO_4$ electrolyte. When VO_2(B) was cycled in $Al_2(SO_4)_3$ electrolyte, an extremely strong anodic peak at around 0.08 V was observed in the first charging process, which is in agreement with that reported by Cai *et al.*[36] on an aqueous aluminum ion battery using a VO_2(B) cathode and implies an Al^{3+} de-intercalation process. It is interesting to note that this peak diminished dramatically during the subsequent charge–discharge processes (as shown in Fig. S9(a)†), thus indicating the unstable structure of VO_2(B) when cycled in $Al_2(SO_4)_3$ electrolyte which is easily destroyed and may be attributed to the high polarizing power of Al^{3+} (Fig. 1(i)).

The electrochemical performances of the as-prepared VO_2(B) in different electrolytes were further evaluated by galvanostatic charge–discharge measurements at different current densities, with the results shown in Fig. 2(b) and Fig. S10.† The nonlinear charge–discharge curves indicate a typical behavior that involves redox reactions,[4] which is in keeping with the CV redox peaks. Notably, the GCD profiles of VO_2(B) cycled in $ZnSO_4$ electrolyte exhibit obvious sloping plateaus (especially at low current density), which may correlate with its different charge storage mechanism that involves phase changes of the electrode material. Fig. 2(c) and Table S3† show the specific capacitances of the as-prepared VO_2(B) cycled in different electrolytes as a function of different current densities and are calculated by using the following equation:[4,14]

$$C = \frac{I\Delta t}{m\Delta V} \quad (1)$$

Where C (F g^{-1}) is the specific capacitance, I (A) is the constant discharge current, Δt (s) is the discharge time, ΔV (V) is the potential window, and m (g) is the mass of the active material in the electrode. Noteworthily, it is found that although the rate capabilities are similar when VO_2(B) is cycled in Na_2SO_4, $MgSO_4$ and $ZnSO_4$ electrolytes, the obtained specific capacitances are dramatically different. At 1 A g^{-1} current density, the specific capacitance of VO_2(B) obtained in $ZnSO_4$ electrolyte is 460 F g^{-1}, which is 2.1 times higher than that cycled in Na_2SO_4 electrolyte (218 F g^{-1}) and 2.6 times higher than that cycled in $MgSO_4$ electrolyte (180 F g^{-1}). The significantly enhanced charge storage capability of VO_2(B) in $ZnSO_4$ electrolyte could be attributed to its different charge storage mechanism, which has been implied by CV and GCD measurements and will also be discussed in more detail in the next section. Moreover, the specific capacitances of VO_2(B) obtained in $Al_2(SO_4)_3$ electrolyte are smaller than those obtained in the other three electrolytes (especially at high current densities), which is mainly due to the collapsed structure of VO_2(B) with Al^{3+} (de-)intercalation as reflected from the CV tests and is also confirmed later. EIS measurements were also employed to understand the charge transfer kinetics of VO_2(B) in different electrolytes, with the results shown in Fig. 2(d) and Fig. S11.† All plots exhibit a straight line in the low frequency region and a single semicircle in the high-frequency region, indicating a diffusion-limited step in the low frequency region and a charge transfer limited step in the high-frequency region.[59,60] The Nyquist plots were modeled and interpreted by using an appropriate electrical equivalent circuit, which is shown in the inset in Fig. 2(d). Clearly, it was found that the charge transfer resistance (R_{ct}) increased with increasing the charge numbers of electrolyte cations in a linear trend (Fig. 2(e)). To further understand the mono/multi-valent cations' intercalation behaviors, we turn to the reaction kinetics. Generally speaking, the response current (i) of CVs obeys a power law relationship with the scan rate (v) according to eqn (2):[61,62]

$$i = av^b \quad (2)$$

where a and b are variable parameters, and the b-values can be determined from the slope of linear fit of the $\log(i)$ *vs.* $\log(v)$ plot at a fixed potential (V). In particular, the b-value offers a critical

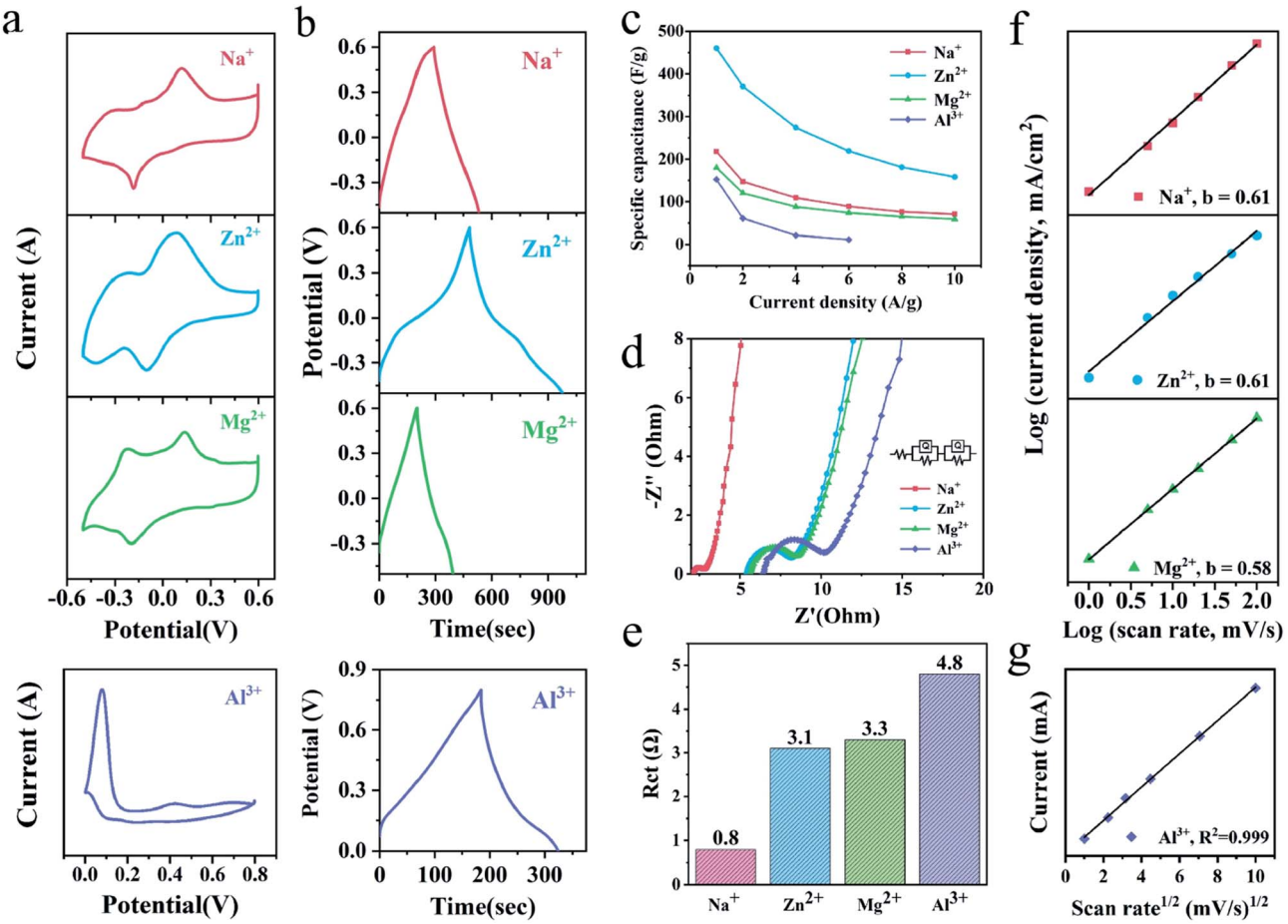

Fig. 2 Electrochemical analysis of VO_2(B) cycled in Na_2SO_4, $MgSO_4$, $ZnSO_4$ and $Al_2(SO_4)_3$ electrolytes. (a) Cyclic voltammetry curves measured at 1 mV s^{-1} scan rate, (b) galvanostatic charge–discharge curves measured at 1 A g^{-1} current density, (c) specific capacitances at various current densities, (d) Nyquist plots (inset: the electrical equivalent circuit used for fitting the impedance spectra), (e) comparison of charge transfer resistances, (f) variation of log(*i*) *vs.* log(*v*) for power law ($i = av^b$) fitted at peak potentials to their *b*-values (Na^+, Zn^{2+} and Mg^{2+}), and (g) the linear dependence of anodic currents with the square root of scan rate for VO_2(B) cycled in $Al_2(SO_4)_3$ electrolyte.

insight into the charge storage mechanism; that is, $b = 0.5$ and 1 indicate diffusion-controlled and surface-controlled processes, respectively. As shown in Fig. 2(f), the *b*-values (obtained by using the anodic peaks at ~0.15 V) are around 0.6 for VO_2(B) cycled in Na_2SO_4, $MgSO_4$ and $ZnSO_4$ electrolytes, indicating mixed kinetic behaviors of the surface-controlled and the intercalation process, with the diffusion-controlled process being dominant, and are consistent with their rate performance. When cycled in $Al_2(SO_4)_3$ electrolyte, the linear relationship between anodic currents and the square root of scan rate ($v^{1/2}$) in the range from 1 to 100 mV s^{-1} (Fig. 2(g)) clearly demonstrates that the aluminum ion insertion is a diffusion controlled process.[60]

In general, the electrochemical analysis reveals distinct charge–discharge behaviors of VO_2(B) with mono/multi-valent cation intercalation, including: (i) significantly improved charge storage capability was obtained when VO_2(B) was cycled in $ZnSO_4$ compared to that cycled in $MgSO_4$, indicating the presence of different charge storage mechanisms since both Zn^{2+} and Mg^{2+} show similar charge numbers, ionic radii and polarizing power; (ii) Mg^{2+} ion insertion should result in higher capacitance due to the accompanying two-electron transfers compared to Na^+ ion intercalation upon cycling. However, our electrochemical results show that the VO_2(B) cycled in both electrolytes exhibit similar charge storage performance, which is likely due to the synergistic effects between the ionic radius of electrolyte cations and their polarizing power; (iii) the structural reason for the inferior electrochemical properties of VO_2(B) cycled in $Al_2(SO_4)_3$ electrolyte should be further elucidated.

3.3 Charge storage mechanism investigation

In order to gain deeper insights into the charge storage mechanisms of mono/multi-valent cation intercalation into VO_2(B), a series of *ex situ* studies (XRD, Raman, SEM and XPS) were carried out on the as-prepared samples at fully charged and discharged states (first cycle, 1 mV s^{-1} scan rate). The electrode materials were scratched off for XRD analysis (since the intense Ni peaks make it difficult to directly detect samples on Ni foam, as shown in Fig. S12†), and the coated Ni foams were directly used for SEM, Raman and XPS measurements. *Ex situ* XRD

patterns of VO_2(B) obtained at fully discharged and charged states are first presented to study the structural changes upon cycling (Fig. 3(a–d)). Compared to the pristine electrode, negative shifts of the (110) diffraction peaks were observed for VO_2(B) after being fully discharged in both Na_2SO_4 and $MgSO_4$ electrolytes, suggesting lattice expansions that correspond to Na^+ and Mg^{2+} intercalation during the discharge process. Interestingly, it is found that the diffraction patterns at the fully discharged state become sharper and stronger, which is likely because the intercalated cations make the arrangement of V and O more orderly because of the interaction among the three ionic species,[33] thus further indicating that the charge storage mechanism of VO_2(B) in Na_2SO_4 and $MgSO_4$ electrolytes is mainly attributed to the cation intercalation. At the fully charged state, the crystallinity of VO_2(B) was found to decrease dramatically, seeing that the intensities of the main diffraction peaks are weakened and several weak peaks have disappeared. It is believed that the inserted ions interact with the host structure, and upon de-intercalation, the local structures of VO_2(B) are likely to be distorted since the Na^+ ion possesses a large ionic size and the Mg^{2+} ion exhibits large polarizing power/strong interaction with the host structure, thus leading to the observed amorphization upon re-charging which has seldom been reported before. It is reasonable to suppose that the de-intercalation of Na^+ and Mg^{2+} ions may simply induce a local structure variation instead of severely destroying the long-range atomic ordering. For the VO_2(B) cycled in $ZnSO_4$ electrolyte, a series of new reflections at 2θ values of about 12.2, 20.1, 20.8, 30.1, 33.9, 36.3, 42.5 and 52.0 emerged at the fully discharged state, which can be assigned to the $Zn_3(OH)_2V_2O_7\cdot 2H_2O$ phase (ICDD Card no. 50-0570) with a much larger interlayer spacing.[34,63] It is also reasonable to assume that the desolvation of zinc may not be necessary since the large interlayer of the new phase could accommodate the hydrated zinc ion, and is thus beneficial for facilitating zinc ion diffusion. During the subsequent charging process, the reflections corresponding to $Zn_3(OH)_2V_2O_7\cdot 2H_2O$ completely disappear at the fully charged state, suggesting the reversible structural evolution and is consistent with the electrochemical results. In addition, the peak positions of VO_2(B) were also shifted toward lower 2θ angles upon discharging, indicating that Zn^{2+} intercalation into VO_2(B) also occurs. Therefore, it is demonstrated that the VO_2(B) experiences a reversible conversion reaction to $Zn_3(OH)_2V_2O_7\cdot 2H_2O$ in $ZnSO_4$ electrolyte, followed by Zn^{2+} (de-)intercalation into both phases upon cycling, thus enabling full utilization of the bulk electrode and thereby leading to its superior charge storage properties.[3] Finally, when Al^{3+} serves as an electrolyte cation, an obvious broadening of the main diffraction peaks and the vanishing of weak diffraction peaks have been observed, along with the presence of an unidentified peak at ~20° that may correlate with Al^{3+} intercalation, thus implying the strong deformation of VO_2(B)'s crystal structure that is mainly due to the large polarizing power of Al^{3+} ions and is in keeping with the electrochemical test results.

More details of the local structural evolution of VO_2(B) were revealed by Raman spectra, with the results shown in Fig. 3(e–h). For the electrodes cycled in Na_2SO_4 and $MgSO_4$ electrolytes, similar variations of the Raman spectra have been observed

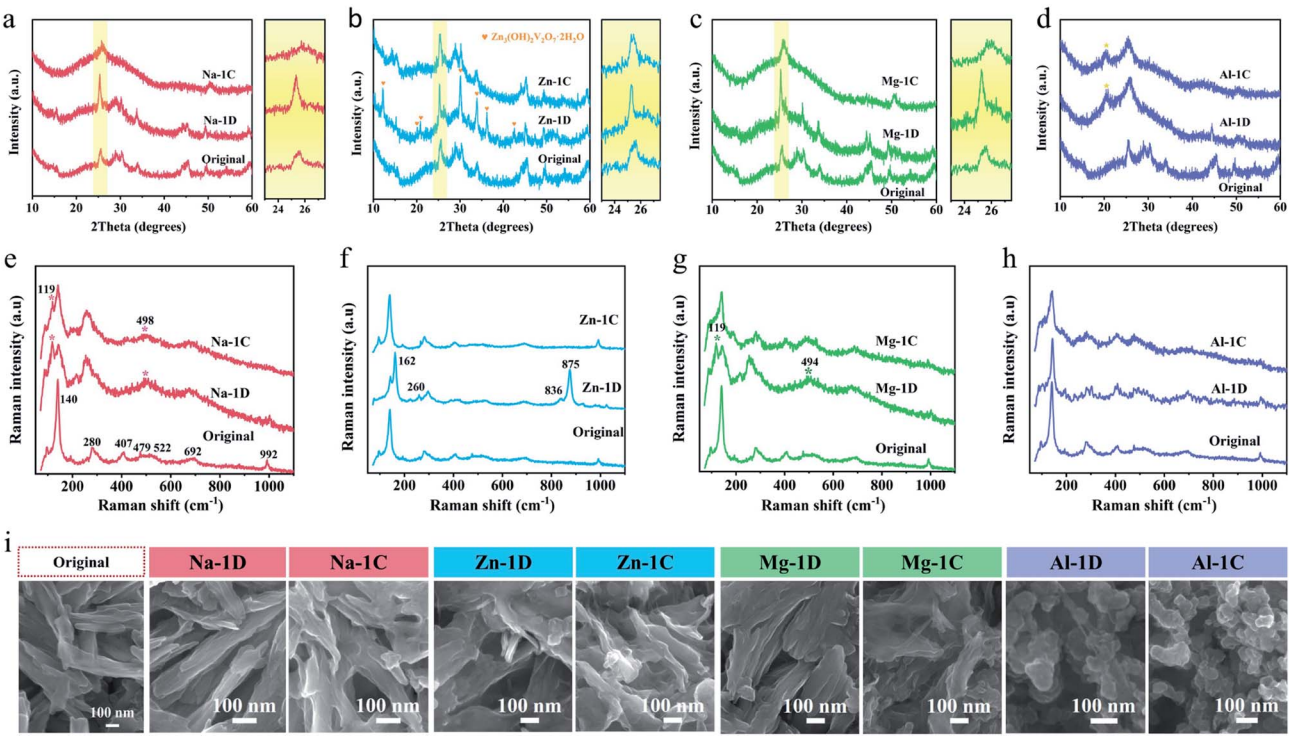

Fig. 3 *Ex situ* (a–d) XRD, (e–h) Raman, and (i) SEM analysis of VO_2(B) cycled in Na_2SO_4, $MgSO_4$, $ZnSO_4$ and $Al_2(SO_4)_3$ electrolytes at fully charged and discharged states (the XRD pattern, Raman spectrum and SEM image of the uncycled VO_2(B) are also included for ease of comparison).

from the pristine to the fully discharged state, including the emergence of two new peaks centered at ~119 and ~494 cm^{-1}, the disappearance of peaks located at 457, 479 and 522 cm^{-1}, the shifts of peaks at 191, 280 and 692 cm^{-1}, and the broadening of all features, which can be attributed to the interactions of intercalated Na^+ and Mg^{2+} ions with VO_2(B) and is consistent with the XRD results. It is interesting to note that although Na^+ and Mg^{2+} exhibit different physicochemical properties, the changes of Raman peaks upon ion insertion are quite similar, which is also consistent with the electrochemical results. The observed Raman spectra variations are partially recovered after being fully charged, meaning that the Na^+ and Mg^{2+} intercalation/de-intercalation processes are not fully reversible for VO_2(B), which were also found in other vanadium oxides.[51] Surprisingly, better reversibility has been found for VO_2(B) cycled in $MgSO_4$ electrolyte, although the low mass Mg^{2+} mobility within the bulk lattice is typically reported due to its large polarizing power (Fig. 1(i)). Thus, the above *ex situ* Raman observations may indicate that different amounts of Na^+ and Mg^{2+} ions are intercalated into the tunnels. Specifically, hard desolvation of the hydrated magnesium results in a smaller amount of bare Mg^{2+} ions, and the large polarizing power of Mg^{2+} leads to a strong interaction with oxygen in VO_2(B) upon discharging and therefore prohibits deep penetration into the bulk of the host structure. In contrast, easy desolvation of the hydrated sodium leads to a larger amount of bare Na^+ ions, while most of them are able to diffuse into the bulk of VO_2(B) because of its smaller polarizing power.[64] However, a lot of Na^+ ions may not be able to easily escape during the re-charging process because of the long diffusion pathway and crowded tunnel gallery, thus resulting in inferior reversibility. This may also explain their similar electrochemical performance, meaning that although Mg^{2+} ions induce two-electron transfers upon cycling, the intercalation amount of Na^+ ions is much larger, thus leading to their comparable charge storage capability. When VO_2(B) was cycled in $ZnSO_4$ electrolyte, several new features emerged at 162, 260, 836 and 875 cm^{-1} at the fully discharged state that could be attributed to the $Zn_3(OH)_2V_2O_7 \cdot 2H_2O$ phase.[63] During the subsequent charging process, the Raman peaks of $Zn_3(OH)_2V_2O_7 \cdot 2H_2O$ completely disappeared at the fully charged state, indicating good reversibility of the phase transformation which is consistent with the XRD results. Moreover, obvious peak shifts have been observed upon discharging, indicating the intercalation of Zn^{2+} ions. Finally, when VO_2(B) was cycled in $Al_2(SO_4)_3$ electrolyte, it was found that the main Raman peaks are still preserved, indicating stable local structures even if the long-range atomic ordering has been destroyed as indicated by XRD. The Raman spectrum of VO_2(B) at the fully discharged state is similar to the pristine one, while an obvious broadening of the Raman features has been observed in the re-charging process, indicating that Al^{3+} de-intercalation is more likely to distort VO_2(B)'s crystal structure.

The SEM images of VO_2(B) cycled in different electrolytes and obtained at fully charged and discharged states were compared, and are shown in Fig. 3(i). Clearly, it can be seen that the samples cycled in Na_2SO_4, $MgSO_4$ and $ZnSO_4$ electrolytes preserve the sheet-like morphology without obvious deterioration, implying that intercalation/de-intercalation of Na^+, Mg^{2+} and Zn^{2+} ions has little effect on VO_2(B)'s morphologies. However, significant morphological change has been observed for VO_2(B) with Al^{3+} ion intercalation. The large-sized VO_2(B) nanobelts in the pristine sample were completely destroyed during the first discharge process, with the formation of small pellets and the lateral dimensions are in the range of 40–60 nm, which is maintained during the subsequent charging process. The irreversible morphology variation of VO_2(B) cycled in $Al_2(SO_4)_3$ electrolyte is in accordance with our previous results and other reported studies, demonstrating severe structural deformation caused by the strong electrostatic force between Al^{3+} ions and the host structure, which also explains its inferior charge storage properties. *Ex situ* XPS analysis was also performed directly on the as-prepared electrodes at fully charged and discharged states to further elucidate their charge storage mechanisms. Clearly, the V $2p_{3/2}$ bands of fully discharged VO_2(B) cycled in Na_2SO_4, $MgSO_4$ and $ZnSO_4$ electrolytes shifted to lower binding energies compared with uncycled ones (Fig. 4(a–c)), while the Na and Mg 1s peaks at 1071.8 and 1304.6 eV and the Zn 2p peaks at 1022.2 and 1045.3 eV can be observed (Fig. S13(a–c)†),[32,51,65] indicating decreased oxidation states of V with ion intercalation. The strong Zn 2p signals (Fig. S13(b)†) at the fully discharged state also indicates the formation of the $Zn_3(OH)_2V_2O_7 \cdot 2H_2O$ phase and is consistent with our previous results. In the re-charging process, the Na and Mg 1s peaks, as well as Zn 2p peak, are still present, demonstrating that the intercalation/de-intercalation processes of the Na^+, Mg^{2+} and Zn^{2+} ions are not fully reversible and some of the cations are captured after being charged. However, the dramatic decrease of Zn 2p peak intensities indicates good reversibility of the phase transformation in $ZnSO_4$ electrolyte. It is noted that the energy shift of the V $2p_{3/2}$ peak in VO_2(B) cycled in $ZnSO_4$ electrolyte is comparable to those cycled in Na_2SO_4 and $MgSO_4$ electrolytes, despite their obviously different specific capacitances. This is likely due to the fact that the as-formed $Zn_3(OH)_2V_2O_7 \cdot 2H_2O$ with a much larger interlayer spacing enables Zn^{2+} ion diffusion into the bulk electrode, whereas XPS is a surface sensitive technique and therefore not able to detect those oxidation state changes occurring in the bulk. Finally, the unnoticeable shift of the V $2p_{3/2}$ peak (Fig. 4(d)) and low intensity of the Al 2p peak (Fig. S13(d)†)[36] have been observed with Al^{3+} ion intercalation, except the fact that the capacitance of VO_2(B) cycled in $Al_2(SO_4)_3$ electrolyte at a low scan rate is non-negligible. This could be attributed to the extremely deformed structure of the active material upon first discharging, and shallow intercalation of the Al^{3+} ion into VO_2(B) tunnels that leads to inhomogeneous changes of the vanadium oxidation state, all together making it hard to discern the oxidation state change of vanadium *via* XPS. Further analyzing the oxygen-containing bonds gives more detailed insights (Fig. 4(e–h)). The characteristic O 1s peaks representing –OH and H–O–H bonds[32,36] in the fully discharged VO_2(B) cycled in Na_2SO_4, $MgSO_4$ and $ZnSO_4$ electrolytes are stronger relative to the initial states (Fig. 4(i–k)), suggesting proton insertion into VO_2(B) along with the Na^+ and Mg^{2+} ions, as well as the formation of the $Zn_3(OH)_2V_2O_7 \cdot 2H_2O$ phase with the Zn^{2+} ion intercalation.

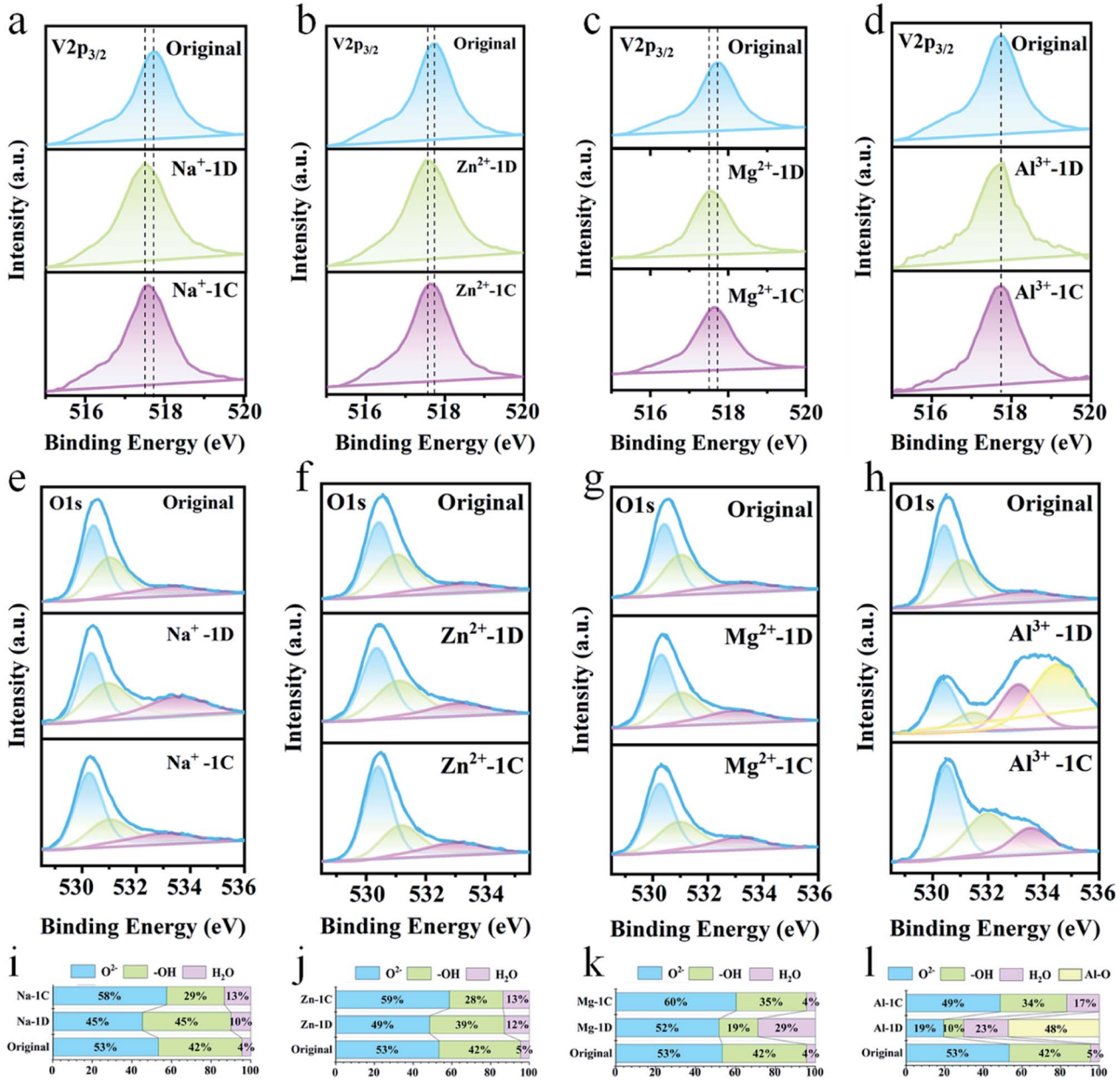

Fig. 4 *Ex situ* XPS spectra of (a–d) V 2p and (e–h) O 1 s of VO_2(B) cycled in Na_2SO_4, $MgSO_4$, $ZnSO_4$ and $Al_2(SO_4)_3$ electrolytes at fully charged and discharged states (the XPS spectra of uncycled VO_2(B) are also included for ease of comparison). (i–l) Comparison of the relative contents of various oxygen-containing bonds.

Interestingly, an obvious peak centered at about 534.3 eV is observed for VO_2(B) cycled in $Al_2(SO_4)_3$ electrolyte, which is attributed to the bridging oxygen atoms involving Al ions.[66] Therefore, the above results further confirm the strong electrostatic interaction between Al^{3+} ions and the host structure, which is the intrinsic reason for complete deformation of the long-range atomic structure of VO_2(B).

To further understand the mono/multi-valent cation intercalation into VO_2(B), we have performed DFT calculations to examine the adsorption energies of Na, Mg, Zn and Al on VO_2(B)'s surfaces, with the results shown in Fig. 5(a–d) and Table S4.† Negative adsorption energy values are observed for all four cations, indicating their favorable adsorption on the VO_2(B) surface. Specifically, the Al^{3+} ion exhibits the largest adsorption energy (−8.17 eV), which is in accordance with its high polarizing power and indicates strong chemical bonds between Al and O. Such a strong interaction may impede Al^{3+} desorption and furthermore destroy the lattice structure, thus resulting in serious structural instability and is consistent with our previous experimental results. Moderate adsorption energies of Na^+ (−3.39 eV) and Mg^{2+} (−4.78 eV) have been obtained, which also correlate well with their polarizing power, therefore demonstrating weakened interaction of Na and Mg with lattice oxygen compared to Al, leading to enhanced ion intercalation

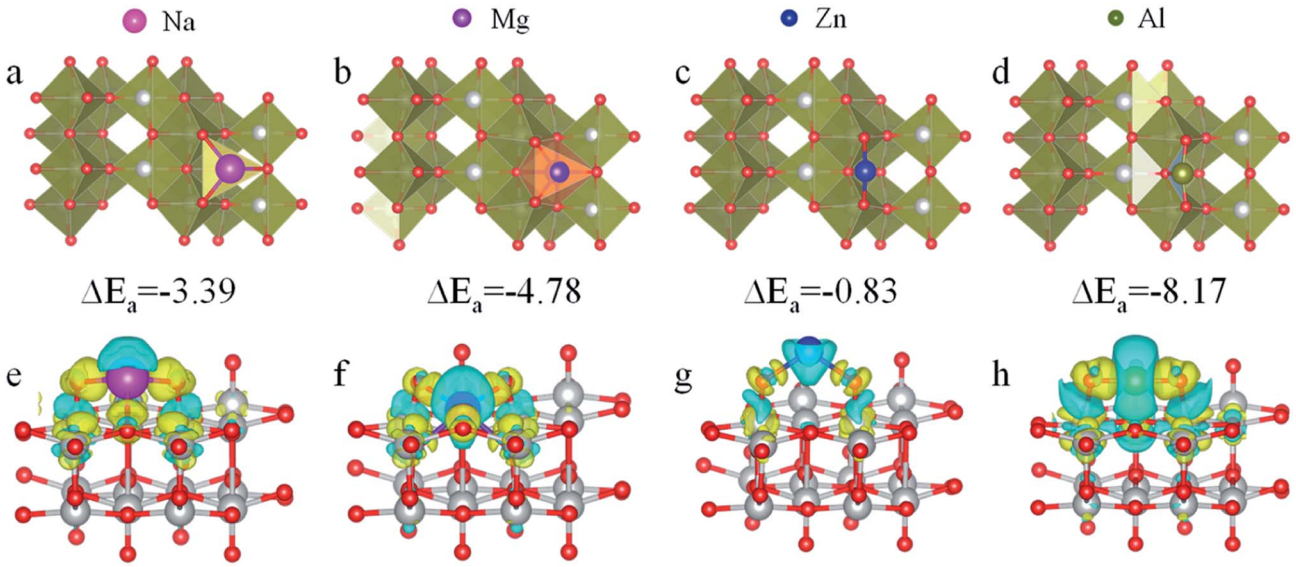

Fig. 5 The optimized structural geometry of (a) Na, (b) Mg, (c) Zn, and (d) Al adsorbed on the VO_2(B) surface and their adsorption energies. Side views of the deformation charge density for (e) Na, (f) Mg, (g) Zn, and (h) Al adsorbed on the VO_2(B) surface. Color code: grey spheres for V and red spheres for oxygen.

into the tunnels (especially for the Na^+ ion) which has been confirmed experimentally. Surprisingly, the Zn^{2+} ion exhibits the smallest adsorption energy (−0.83 eV) except the fact that it possesses high polarizing power, which signifies the most favorable intercalation of the Zn^{2+} ion into VO_2(B). Moreover, we have calculated the standard Gibbs free energy change during the formation process of $Zn_3(OH)_2V_2O_7$ according to the formula:

$$\Delta G = \Delta E_{\text{tol}} + \Delta E_{\text{zpe}} - T\Delta S - eU \quad (3)$$

where $\Delta E_{\text{tol}}(n)$, $\Delta E_{\text{zpe}}(n)$ and $\Delta S(n)$ representing the corresponding reaction are the DFT total energy difference, zero point correction energy difference, and entropy change under standard conditions (T = 298 K). As shown in Table S5,† the negative ΔG value clearly indicates thermodynamically favorable formation of $Zn_3(OH)_2V_2O_7$ in the presence of VO_2 and Zn^{2+} ions. Thus, the above calculation results demonstrate the facile insertion of Zn^{2+} into VO_2(B) and ease of formation of the $Zn_3(OH)_2V_2O_7$ phase, which is consistent with our structural characterization and electrochemical analysis. In order to further understand the interaction between adsorbed cations and VO_2(B) during the insertion process, we have calculated the distribution of the deformation charge density by using the formula:

$$\Delta\rho = \rho_{AB} - \rho_A - \rho_B \quad (4)$$

where ρ_{AB} represents the total charge density of VO_2(B) containing one adsorbed atom, ρ_A and ρ_B are the charge density of isolated VO_2(B) and the electrolyte cation while maintaining the same positions/coordinates for all atoms in the system.[67,68] The yellow and blue regions correspond to enrichment and depletion of electron density, respectively. An obvious charge transfer occurred between all adsorbed atoms and the VO_2(B) layer. The adsorbed atoms lose electrons (corresponding to the blue region) while the nearby O and V receive electrons (corresponding to the yellow region) as illustrated in Fig. 5(e–h). Meanwhile, different distributions of the deformation charge density imply different bonding situations between the adsorbed atoms and host structure. Fig. 5(h) shows a large blue region around the Al ion, a large yellow region around lattice oxygen and direct large area contact of the electron emergence region between Al and O, which implies a strong interaction between them due to a large number of transferred electrons[69] and is in line with its large adsorption energy. Similar bonding situations have been observed for Na and Mg adsorbed VO_2(B) (Fig. 5(e and f)), except their smaller number of transferred electrons, and therefore manifests their weaker interaction compared to the Al adsorption system. Moreover, a discontinuous region of electrons appears between Zn and O, while a small yellow region around lattice oxygen has been observed (Fig. 5(g)), indicating extremely weak interaction between adsorbed Zn and lattice oxygen.[69] Therefore, the distributions of deformation charge density are consistent with the calculated adsorption energies for Na, Mg, Zn and Al adsorbed VO_2(B), which further confirms their different intercalation behaviors.

Based on the above discussions, the charge storage mechanisms of VO_2(B) cycled in the four different electrolytes can be illustrated as follows (Fig. 6). The ion (de-)intercalation into the tunnels, accompanied by the V oxidation state change, is the main charge storage mechanism for VO_2(B) cycled in Na_2SO_4 and $MgSO_4$ electrolytes. However, different amounts of Na^+ and Mg^{2+} ions are intercalated into VO_2(B) tunnels due to the synergistic effects between the ionic radius of electrolyte cations and their polarizing power, which explains their comparable charge storage capability. In contrast, part of VO_2(B) is

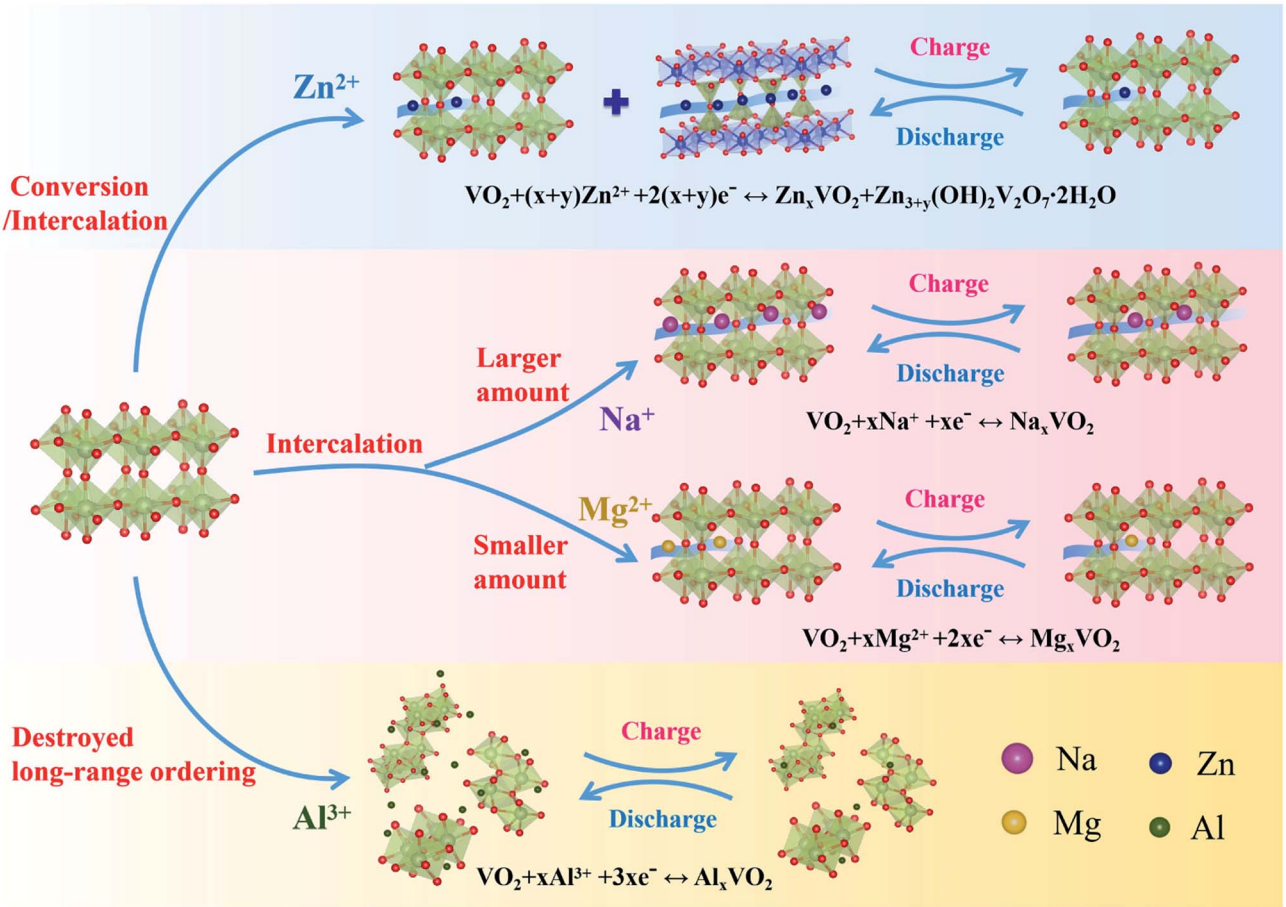

Fig. 6 Schematic illustration of the charge storage mechanisms of VO_2(B) cycled in Na_2SO_4, $MgSO_4$, $ZnSO_4$ and $Al_2(SO_4)_3$ electrolytes.

reversibly converted to $Zn_3(OH)_2V_2O_7\cdot 2H_2O$ when added to $ZnSO_4$ electrolyte, followed by Zn^{2+} ion (de-)intercalation into both phases during the charge–discharge processes, thus enabling full utilization of the bulk electrode and leading to its superior specific capacitance. Moreover, the large VO_2(B) nanobelts collapse into small pellets when cycled in $Al_2(SO_4)_3$ electrolyte, which is attributed to the strong electrostatic force between Al^{3+} ions and the host structure, therefore resulting in severe structural instability and inferior pseudocapacitive properties.

4. Conclusions

In summary, we have systematically investigated the behaviors of Na^+, Mg^{2+}, Zn^{2+} and Al^{3+} upon intercalation into VO_2(B) through a series of structural characterization experiments, theoretical calculations and electrochemical analysis. It is found that only ion (de-)intercalation into VO_2(B) occurs in Na_2SO_4 and $MgSO_4$ electrolytes upon cycling (with different amounts of Na^+ and Mg^{2+} ions intercalated into the tunnels), and their distinct charge storage properties are mainly attributed to the synergistic effects between the ionic radius of electrolyte cations and their polarizing power. In contrast, part of VO_2(B) is reversibly converted to $Zn_3(OH)_2V_2O_7\cdot 2H_2O$ in $ZnSO_4$ electrolyte due to easy transformation to the new phase, along with Zn^{2+} (de-)intercalation into both phases upon cycling, thus enabling full utilization of the bulk electrode and leading to superior charge storage capability. When cycled in $Al_2(SO_4)_3$ electrolyte, the large VO_2(B) nanobelts collapse into small pellets, which is mainly due to the strong electrostatic force between Al^{3+} ions and the host structure, thus resulting in serious structural instability and inferior pseudocapacitive properties. In general, the detailed experimental comparisons and theoretical calculations demonstrated in our work provide valuable insights in the mechanistic understanding of the mono/multi-valent cations' intercalation into VO_2(B), which is beneficial for the rational design of more layered oxides with excellent electrochemical performance or will be extended to other applications.

Author contributions

Y. Zeng carried out the sample synthesis, electrochemical measurements and structural analysis. J. Hu and K. K. Guo did the theoretical calculations. J. F. Yang, P. Tang, Y. F. Peng and P. T. Xiao did the electrochemical/structural analysis. Q. F. Fu did the XRD measurement. W. Zhou did the Raman measurement. S. Chen did the XPS measurement. P. Gao, H. L. Dong and J. L. Liu supervised the whole project. All the authors contributed to manuscript preparation.

Conflicts of interest

There are no conflicts of interest to declare.

Acknowledgements

This work was financially supported by the National Natural Science Foundation of China (22075074, U21A2081), Outstanding Young Scientists Research Funds from Hunan Province (2020JJ2004), Major Science and Technology Program of Hunan Province (2020WK2013), Natural Science Foundation of Hunan Province (2020JJ5035), and Macau Science and Technology Development Fund (Macau SAR, FDCT-0096/2020/A2).

References

1 P. Poizot, J. Gaubicher, S. Renault, L. Dubois, Y. Liang and Y. Yao, *Chem. Rev.*, 2020, **120**, 6490–6557.
2 S. Chen, L. Qiu and H.-M. Cheng, *Chem. Rev.*, 2020, **120**, 2811–2878.
3 P. Gao, Y. Zeng, P. Tang, Z. Wang, J. Yang, A. Hu and J. Liu, *Adv. Funct. Mater.*, 2022, **32**, 2108644.
4 P. Gao, P. Metz, T. Hey, Y. Gong, D. Liu, D. D. Edwards, J. Y. Howe, R. Huang and S. T. Misture, *Nat. Commun.*, 2017, **8**, 14559.
5 R. Zhao, L. Zhang, C. Wang and L. Yin, *J. Power Sources*, 2017, **353**, 77–84.
6 X. Yu, S. Yun, J. S. Yeon, P. Bhattacharya, L. Wang, S. W. Lee, X. Hu and H. S. Park, *Adv. Energy Mater.*, 2018, **8**, 1702930.
7 L. Kong, C. Zhang, J. Wang, W. Qiao, L. Ling and D. Long, *ACS Nano*, 2015, **9**, 11200–11208.
8 D. Liu and G. Cao, *Energy Environ. Sci.*, 2010, **3**, 1218–1237.
9 M. Lee, B.-H. Wee and J.-D. Hong, *Adv. Energy Mater.*, 2015, **5**, 1401890.
10 Z. Khan, P. Singh, S. A. Ansari, S. R. Manippady, A. Jaiswal and M. Saxena, *Small*, 2021, **17**, 2006651.
11 H. Wang, H. Yi, X. Chen and X. Wang, *J. Mater. Chem. A*, 2014, **2**, 1165–1173.
12 Y. Zhang, J. Zheng, T. Hu, F. Tian and C. Meng, *Appl. Surf. Sci.*, 2016, **371**, 189–195.
13 Y. Liu, Y. Zhang, T. Hu, Y. Mu, J. Sun, J. Zheng, H. Jiang, X. Dong and C. Meng, *Colloids Surf. A*, 2020, **586**, 124222.
14 P. Gao, R. J. Koch, A. C. Ladonis and S. T. Misture, *J. Electrochem. Soc.*, 2020, **167**, 160523.
15 C. Nethravathi, B. Viswanath, J. Michael and M. Rajamath, *Carbon*, 2012, **50**, 4839–4846.
16 M. S. Kang, S. K. Park, P. Nakhanivej, K. H. Shin, J. S. Yeon and H. S. Park, *J. Alloys Compd.*, 2021, **855**, 157361.
17 S. Yang, Y. Gong, Z. Liu, L. Zhan, D. P. Hashim, L. Ma, R. Vajtai and P. M. Ajayan, *Nano Lett.*, 2013, **13**, 1596–1601.
18 C. Xia, Z. Lin, Y. Zhou, C. Zhao, H. Liang, P. Rozier, Z. Wang and H. N. Alshareef, *Adv. Mater.*, 2018, **30**, 1803594.
19 N. Jabeen, A. Hussain, Q. Xia, S. Sun, J. Zhu and H. Xia, *Adv. Mater.*, 2017, **29**, 1700804.
20 Z. Peng, J. Huang, Q. He, S. Li, L. Tan and Y. Chen, *J. Mater. Chem. A*, 2021, **9**, 14363–14371.
21 Z. Peng, J. Huang, Y. Wang, K. Yuan, L. Tan and Y. Chen, *J. Mater. Chem. A*, 2019, **7**, 27313–27322.
22 L. Gu, J. Wang, J. Ding, B. Li and S. Yang, *Electrochim. Acta*, 2019, **295**, 393–400.
23 C. Niu, J. Meng, C. Han, K. Zhao, M. Yan and L. Mai, *Nano Lett.*, 2014, **14**, 2873–2878.
24 P. Liu, Y. Xu, K. Zhu, K. Bian, J. Wang, X. Sun, Y. Gao, H. Luo, L. Lu and J. Liu, *J. Mater. Chem. A*, 2017, **5**, 8307–8316.
25 M.-S. Balogun, Y. Luo, F. Lyu, F. Wang, H. Yang, H. Li, C. Liang, M. Huang, Y. Huang and Y. Tong, *ACS Appl. Mater. Interfaces*, 2016, **8**, 9733–9744.
26 G. He, L. Li and A. Manthiram, *J. Mater. Chem. A*, 2015, **3**, 14750–14758.
27 D. Jin, Y. Gao, D. Zhang, Y. Wei, G. Chen, H. Qiu and X. Meng, *J. Alloys Compd.*, 2020, **845**, 156232.
28 Z. Li, Y. Ren, L. Mo, C. Liu, K. Hsu, Y. Ding, X. Zhang, X. Li, L. Hu, D. Ji and G. Cao, *ACS Nano*, 2020, **14**, 5581–5589.
29 Y. Cai, R. Chua, Z. Kou, H. Ren, D. Yuan, S. Huang, S. Kumar, V. Verma, P. Amonpattaratkit and M. Srinivasan, *ACS Appl. Mater. Interfaces*, 2020, **12**, 36110–36118.
30 X. Dai, F. Wan, L. Zhang, H. Cao and Z. Niu, *Energy Storage Mater.*, 2019, **17**, 143–150.
31 Z. Li, S. Ganapathy, Y. Xu, Z. Zhou, M. Sarilar and M. Wagemaker, *Adv. Energy Mater.*, 2019, **9**, 1900237.
32 H. Luo, B. Wang, C. Wang, F. Wu, F. Jin, B. Cong, Y. Ning, Y. Zhou, D. Wang, H. Liu and S. Dou, *Energy Storage Mater.*, 2020, **33**, 390–398.
33 C. Liu, Z. Neale, J. Zheng, X. Jia, J. Huang, M. Yan, M. Tian, M. Wang, J. Yang and G. Cao, *Energy Environ. Sci.*, 2019, **12**, 2273–2285.
34 J. Ding, Z. Du, L. Gu, B. Li, L. Wang, S. Wang, Y. Gong and S. Yang, *Adv. Mater.*, 2018, **30**, 1800762.
35 J. Ding, H. Gao, K. Zhao, H. Zheng, H. Zhang, L. Han, S. Wang, S. Wu, S. Fang and F. Cheng, *J. Power Sources*, 2021, **487**, 229369.
36 Y. Cai, S. Kumar, R. Chua, V. Verma, D. Yuan, Z. Kou, H. Ren, H. Arora and M. Srinivasan, *J. Mater. Chem. A*, 2020, **8**, 12716–12722.
37 J.-M. Li, K.-H. Chang and C.-C. Hu, *Electrochem. Commun.*, 2010, **12**, 1800–1803.
38 C.-C. Hu, C.-M. Huang and K.-H. Chang, *J. Power Sources*, 2008, **185**, 1594–1597.
39 C.-C. Hu and K.-H. Chang, *Electrochem. Solid-State*, 2004, **7**, A400.
40 B. Grégoire, C. Ruby and C. Carteret, *Cryst. Growth Des.*, 2012, **12**, 4324–4333.
41 G. Kresse and J. Furthmüller, *Phys. Rev. B: Condens. Matter Mater. Phys.*, 1996, **54**, 11169–11186.
42 J. P. Perdew, K. Burke and M. Ernzerhof, *Phys. Rev. Lett.*, 1996, **77**, 3865–3868.
43 S. Grimme, J. Antony, S. Ehrlich and H. Krieg, *J. Chem. Phys.*, 2010, **132**, 154104.
44 V. I. Anisimov, F. Aryasetiawan and A. I. Lichtenstein, *J. Phys.: Condens. Matter*, 1997, **9**, 767–808.
45 Z. Sun, T. Liao, Y. Dou, S. M. Hwang, M.-S. Park, L. Jiang, J. H. Kim and S. X. Dou, *Nat. Commun.*, 2014, **5**, 3813.

46 S. Zhang, Y. Li, C. Wu, F. Zheng and Y. Xie, *J. Phys. Chem. C*, 2009, **113**, 15058–15067.
47 G. Nie, X. Lu, Y. Zhu, M. Chi, M. Gao, S. Chen and C. Wang, *ChemElectroChem*, 2017, **4**, 1095–1100.
48 Y. Zhang, X. Jing, Y. Cheng, T. Hu and M. Changgong, *Inorg. Chem. Front.*, 2018, **5**, 2798–2810.
49 P. Shvets, O. Dikaya, K. Maksimova and A. Goikhman, *J. Raman Spectrosc.*, 2019, **50**, 1226–1244.
50 N. Li, W. Huang, Q. Shi, Y. Zhang and L. Song, *Ceram. Int.*, 2013, **39**, 6199–6206.
51 T. Luo, Y. Liu, H. Su, R. Xiao, L. Huang, Q. Xiang, Y. Zhou and C. Chen, *Electrochim. Acta*, 2018, **260**, 805–813.
52 Y. Pan, Y. Lin, Y. Liu and C. Liu, *Catal. Sci. Technol.*, 2016, **6**, 1611–1615.
53 S. Fu, Q. Fang, A. Li, Z. Li, J. Han, X. Dang and W. Han, *Energy Sci. Eng.*, 2021, **9**, 80–100.
54 Y. Liu, E. Uchaker, N. Zhou, J. Li, Q. Zhang and G. Cao, *J. Mater. Chem.*, 2012, **22**, 24439–24445.
55 C. Wang, M. Wang, L. Liu and Y. Huang, *ACS Appl. Energy Mater.*, 2021, **4**, 1833–1839.
56 K.-H. Chang and C.-C. Hu, *Acta Mater.*, 2007, **55**, 6192–6197.
57 V. Verma, S. Kumar, W. Manalastas, J. Zhao, R. Chua, S. Meng, P. Kidkhunthod and M. Srinivasan, *ACS Appl. Energy Mater.*, 2019, **2**, 8667–8674.
58 F. Cui, J. Zhao, D. Zhang, Y. Fang, F. Hu and K. Zhu, *Chem. Eng. J.*, 2020, **390**, 124118.
59 P. Gao, Y. Gong, N. P. Mellott and D. Liu, *Electrochim. Acta*, 2015, **173**, 31–39.
60 P. Gao and D. Liu, *Sens. Actuators, B*, 2015, **208**, 346–354.
61 J. Duay, S. A. Sherrill, Z. Gui, E. Gillette and S. B. Lee, *ACS Nano*, 2013, **7**, 1200–1214.
62 M. Sathiya, A. S. Prakash, K. Ramesha, J. M. Tarascon and A. K. Shukla, *J. Am. Chem. Soc.*, 2011, **133**, 16291–16299.
63 L. Yang, Y. Tang, L. Tong, H. Zhou, J. Ding, T. Fan and D. Zhang, *Appl. Surf. Sci.*, 2015, **346**, 115–123.
64 P.-Y. Chen, A. Adomkevicius, Y.-T. Lu, S.-C. Lin, Y.-H. Tu and C.-C. Hu, *J. Electrochem. Soc.*, 2019, **166**, A1875.
65 Z.-Y. Yao, G.-Q. Zhang, Z.-H. Li, L.-J. Shen and X.-M. Ren, *CrystEngComm*, 2021, **23**, 6533–6540.
66 O. O. Popoola and W. M. Kriven, *J. Mater. Res.*, 1992, **7**, 1545–1552.
67 N. Khossossi, A. Banerjee, Y. Benhouria, I. Essaoudi, A. Ainane and R. Ahuja, *Phys. Chem. Chem. Phys.*, 2019, **21**, 18328–18337.
68 T. Wu, K. Zhu, C. Qin and K. Huang, *J. Mater. Chem. A*, 2019, **7**, 5612–5620.
69 J. Wang, Q. Zhou, L. Xu, X. Gao and W. Zeng, *Phys. E*, 2020, **118**, 113947.